Front. Phys., 2012, 7(2): 223–234
DOI 10.1007/s11467-012-0247-y

REVIEW ARTICLE

Quantum phase transition of cold atoms trapped in optical lattices

Yao-hua Chen†, **Wei Wu**, **Guo-cai Liu**, **Hong-shuai Tao**, **Wu-ming Liu***

Beijing National Laboratory for Condensed Matter Physics, Institute of Physics, Chinese Academy of Sciences, Beijing 100190, China
E-mail: †*chenyaohua@iphy.ac.cn*, **wmliu@aphy.iphy.ac.cn*
Received November 27, 2011; accepted December 15, 2011

We review our recent theoretical advances in phase transition of cold atoms in optical lattices, such as triangular lattice, honeycomb lattice, and Kagomé lattice. By employing the new developed numerical methods called dynamical cluster approximation and cellular dynamical mean-field theory, the properties in different phases of cold atoms in optical lattices are studied, such as density of states, Fermi surface and double occupancy. On triangular lattice, a reentrant behavior of phase translation line between Fermi liquid state and pseudogap state is found due to the Kondo effect. We find the system undergoes a second order Mott transition from a metallic state into a Mott insulator state on honeycomb lattice and triangular Kagomé lattice. The stability of quantum spin Hall phase towards interaction on honeycomb lattice with spin–orbital coupling is systematically discussed. And we investigate the transition from quantum spin Hall insulator to normal insulator in Kagomé lattice which includes a nearest-neighbor intrinsic spin–orbit coupling and a trimerized Hamiltonian. In addition, we propose the experimental protocols to observe these phase transition of cold atoms in optical lattices.

Keywords quantum phase transition, optical lattice, DMFT, spin–orbit coupling

PACS numbers 03.67.Lx, 03.65.Yz, 03.75.Hh, 05.30.Fk, 82.56.Jn

Contents

1 Introduction

Quantum phase transition in strongly correlated system presents some of most challenging problems. However, in a real material, the kinetic energy and interaction between electrons are hard to be varied. The effects of interest would be complicated by multiple bands and impurities. A new developing technology called optical lattices presents a highly controllable and clean system for studying strongly correlated system, in which the relevant parameter can be adjusted independently [1–9]. Optical lattices with different geometrical properties can be set up by adjusting the propagation directions of laser beams, such as triangular lattice, honeycomb lattice and Kagomé lattice [10–16]. The Feshbach resonance employed in the experiment can adjust the interaction between the trapped atoms, such as ^{6}Li and ^{40}K. Recently, a series of experiments have been carried out to investigate the quantum phase transition of cold atoms

in optical lattices [17–24].

The recent theoretical and experimental progress in laser-induced-gauge-field [25–31] makes it a hot spot to study topological quantum states [32, 33] in cold atomic system [34–42]. Subject to the compounds' natural properties [43], the famous Haldane model [44] has not been confirmed by experiments due to the difficulty of implementing periodic magnetic field on actual material. For topological insulator, an important extension from the Haldane model to a time-reversal invariant system [45–53], only a few materials are confirmed currently to have such exotic topological properties [54–59], because the existence of such properties requires relatively strong spin–orbit coupling. However, in optical lattice system, the lattice Hamiltonian can be engineered to guarantee that this system hosts these novel topological phases [40, 41]. And the spin Chern number can be directly verified by using a method similar to the method used to detect the (mass) Chern number in these atomic systems. Recently, the neutral-cold-atom integer and fractional quantum Hall effects have been studied [60–62] and also the realization of Haldane model has been designed by using the laser-induced-gauge-field method in optical lattice [37]. These systems have been widely investigated [38, 63].

Many analytical and numerical methods have been developed to investigate these strongly correlated systems [64–76]. The dynamical mean-field theory (DMFT) [77] has been proven to be a good approximation even for three dimensional situation [78, 79]. However, in low dimensional system and frustrated system, the nonlocal correlations cannot be simply ignored. With the cluster extension of DMFT, such as dynamical cluster approximation (DCA) [80, 81] and cellular dynamical mean-field theory (CDMFT) [82–84], the spatial correlations can be incorporated effectually and the irreducible quantities of embedded cluster are used as an approximation for corresponding lattice quantities. DCA and CDMFT have been widely employed to investigate the low dimensional and frustrated systems [85, 86].

In this article, we review our recent theoretical advances in phase transition in optical lattices with different geometrical properties and spin–orbit coupling. In Section 2, we present experimental sketches to obtain optical lattice, such as square lattice, triangular lattice, honeycomb lattice and Kagomé lattice. In Section 3, we give a general introduction of the numerical method, such as dynamical cluster theory and cellular dynamical mean-field theory. Section 4 is devoted to investigate the phase transition of cold atoms in triangular optical lattice and interacting Dirac fermions on honeycomb lattice. The phase transition of cold atoms with spin–orbit coupling on honeycomb lattice and Kagomé lattice are also presented. In Section 5, we discuss the experiment protocol to observe the phase transition in optical lattices. Finally, we summarize our results.

2 Optical lattices

2.1 Two-dimensional square optical lattice

As shown in Fig. 1, a two-dimensional (2D) square lattice can be formed by two pairs of laser beams, such as a Yb fibre laser at wavelength $\lambda = 1024$ nm, oriented orthogonally on horizontal x–y plane. An additional vertical optical lattice is applied to provide a vertical confinement, which is formed by two beams at an angle of $\pi/12$. This vertical confinement is kept deep enough to prevent vertical tunnelling. And the cold atoms is loaded into a single site of the vertical lattice [20, 21].

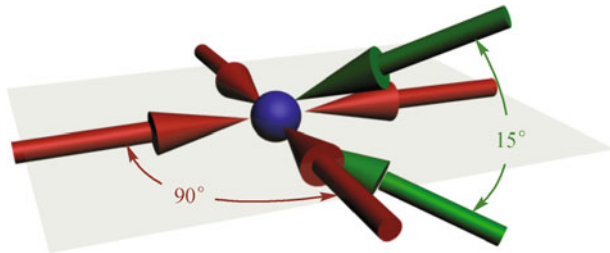

Fig. 1 Sketch map of the experimental setup to form 2D square optical lattice by two pairs of laser beams oriented orthogonally on horizontal x–y plane, which is indicated by the red arrows. Two vertical laser beams, indicated by the green arrows, with $\pi/12$, is applied to prevent vertical tunnelling, which makes the cold atoms load into a single site of the vertical lattice.

2.2 Triangular optical lattice

As shown in Fig. 2(a), the triangular optical lattice can be formed by three laser beams, such as the Yb fiber laser at wavelength $\lambda = 1064$ nm, with a $2\pi/3$ angle between each other. Cold atoms, which can be prepared by mixing two magnetic sub-levels of the $F = 9/2$ hyperfine manifold, are trapped in this triangular optical lattice, such as ^{40}K [20]. Figure 2(b) shows the landscape of the potential of triangular optical lattice in the x–y plane, where the dark blue parts in the figure indicate the minimum lattice potential. Contour lines of the triangular optical lattice are shown in Fig. 2(c). The red dash lines show the geometry of this triangular optical lattice [9, 87].

2.3 Honeycomb optical lattice

The experimental setup of hexagonal optical lattice is illustrated in Fig. 3(a). We can use Yb fiber laser at wavelength $\lambda = 1064$ nm to get three trapping potentials. Each of the potential can be formed by two blue-detuned laser beams at a 70.4° angle, as shown in Fig. 3(a). Then we can get the trapping potential which can be written in the form $V(x, y) = V_0 \sum_{j=1,2,3} \sin^2 [k_L(x \cos \theta_j +$

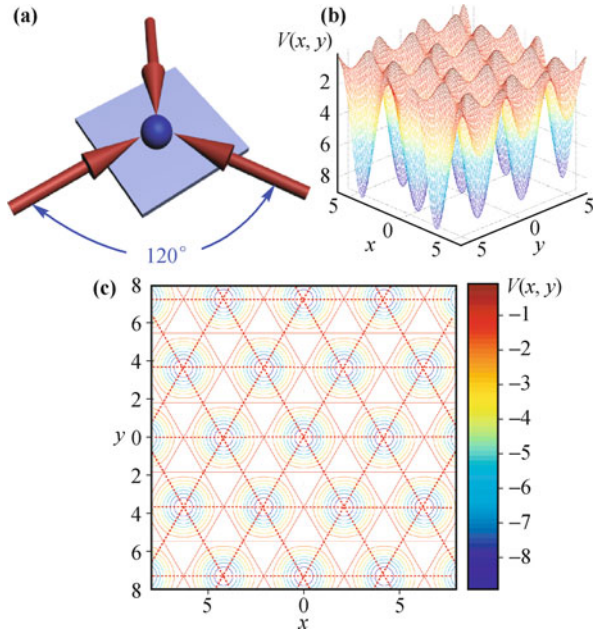

Fig. 2 **(a)** Sketch of experimental setup to form triangular optical lattice. Each arrow depicts a laser beam, the sphere in center of the figure depicts the fermionic quantum gas, such as ^{40}K. **(b)** Landscape of potential $V(x, y)$. **(c)** The contour lines of triangular optical lattice. The dark blue circles indicate the minimum lattice potential. The dash red lines show the geometry of this triangular optical lattice by connecting the minimum lattice potential. Reproduced from Ref. [85], Copyright © 2010 American Physical Society.

$y \sin\theta_j) + \frac{\pi}{2}]$, where $\theta_1 = \frac{\pi}{6}$, $\theta_2 = -\frac{\pi}{6}$, $\theta_3 = \frac{\pi}{2}$, k_L is optical wave vector projected onto x–y plane, V_0 is the depth of the lattice potential [88, 89]. The contour lines of this hexagonal optical lattice are shown in Fig. 3(b), the blue lines indicate the minimum lattice potential. Recently, a spin-dependent optical lattice with hexagonal symmetry has been realized in experiment [90].

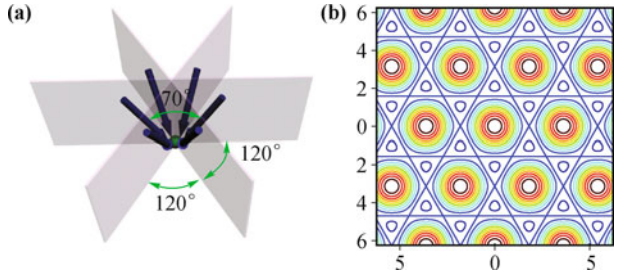

Fig. 3 **(a)** Sketch map of the experimental setup to form hexagonal optical lattice. **(b)** The contourlines of hexagonal optical lattice, the blue lines indicate the minimum lattice potential. The referenced paper is submitted to Chinese Science Bulletin.

2.4 Kagomé optical lattice

The kagomé optical lattice can be formed by three super-laser beams with the same wave vector length but different polarizations. These super-laser beams are applied along three different directions: $\boldsymbol{e}_y$ and $\frac{1}{2}\boldsymbol{e}_y \pm \frac{\sqrt{3}}{2}\boldsymbol{e}_x$, respectively [74, 91, 92]. Each super-laser beam consists of four large detuned standing-wave lasers with the same polarization but different wave vector length in the x–y plane. The total potential is thus given by

$$\begin{aligned} V(\boldsymbol{r}) = V_0 \sum_{i=1}^{3} \{ & \cos(\boldsymbol{k}_i \cdot \boldsymbol{r} + 3\delta_i \varphi/2) \\ & + 2\cos(\boldsymbol{k}_i \cdot \boldsymbol{r}/3 + \delta_i \varphi/2) \\ & + 4\cos(\boldsymbol{k}_i \cdot \boldsymbol{r}/9 + \delta_i \varphi/6) \\ & + \zeta \cos[\boldsymbol{k}_i \cdot \boldsymbol{r}/9 + \delta_i(\varphi/6 + \pi/2)]\}^2 \end{aligned} \quad (1)$$

with the wave vectors $\boldsymbol{k}_1 = \left(\frac{\sqrt{3}}{2}, \frac{1}{2}\right) k$, $\boldsymbol{k}_2 = \left(-\frac{\sqrt{3}}{2}, \frac{1}{2}\right) k$, $\boldsymbol{k}_3 = (0, 1)k$ and $\delta_1 = \delta_2 = -\delta_3 = 1$. One can get a triangular lattice when $\varphi = 0$ or 2π and a Kagomé lattice when $0 < \varphi < 2\pi$. A uniform Kagomé lattice corresponds to $\varphi = \pi$, as shown in Fig. 4(a). When φ takes other values, one can obtain the trimerized Kagomé lattice accompanying distortion of the lattice structure [74, 91, 92]. As shown in Fig. 4(b), the trimerized Kagomé optical lattice is obtained when parameter $\zeta = 1.5$.

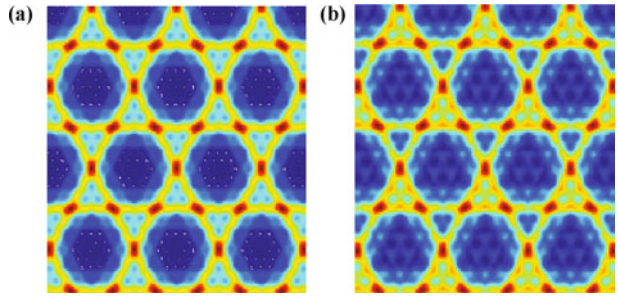

Fig. 4 **(a)** A uniform Kagomé lattice for $\varphi = \pi$ and $\zeta = 0$. **(b)** A trimer Kagomé lattice for $\varphi = \pi$ and $\zeta = 1.5$. Reproduced from Ref. [38], Copyright © 2010 American Physical Society.

2.5 Theoretical model

We first consider the Bose gas trapped in optical lattice [1, 10]. The Hamiltonian of trapped interacting particles can be written as

$$\begin{aligned} H = & \int \mathrm{d}^3 x \hat{\psi}^+(x) \left[\frac{p^2}{2m} + V_0(x)\right] \hat{\psi}(x) \\ & + \frac{g}{2} \int \mathrm{d}x \hat{\psi}^+(x) \hat{\psi}^+(x) \hat{\psi}(x) \hat{\psi}(x) \end{aligned} \quad (2)$$

where $\hat{\psi}$ is the bosonic field operator, V_0 is the optical lattice potential, g is the interaction strength between two atomic particles. By assuming all particles are on the lowest band of the optical lattice, the bosonic field operator can be written as $\hat{\psi}(x) = \sum_i \hat{b}_i w^{(0)}(x - x_i)$, where $\hat{b}_i$ is the destruction operator of particle in site x_i. Then we get the Bose–Hubbard Hamiltonian written as

$$H = -\sum_{i,j} J_{ij} \hat{b}_i^+ \hat{b}_j + \frac{1}{2} \sum_{i,j,k,l} U_{ijkl} \hat{b}_i^+ \hat{b}_j^+ \hat{b}_k \hat{b}_l \quad (3)$$

where

$$J_{ij} = -\int \mathrm{d}x w_0(x - x_i) \left[\frac{p^2}{2m} + V_0(x)\right] w_0(x - x_j) \quad (4)$$

and

$$U_{ijkl} = g\int \mathrm{d}x w_0(x-x_i)w_0(x-x_j)w_0(x-x_k)w_0(x-x_l) \tag{5}$$

Several species of atoms can be trapped in the lattice with different hyperfine states, which can be identified with spin degrees of freedom. For example, a spin 1/2 system can be created from two states $|\downarrow\rangle \equiv |a\rangle$ and $|\uparrow\rangle \equiv |b\rangle$ [10]. By using similar setups mentioned above, the Hamilitonian of interacting fermionic atoms trapped in these optical lattices can be written as

$$H = -t\sum_{\langle ij\rangle\sigma} c^+_{i\sigma}c_{j\sigma} + U\sum_i n_{i\uparrow}n_{i\downarrow} \tag{6}$$

where $c^+_{i\sigma}$ and $c_{i\sigma}$ denote the creation and the annihilation operator of the fermionic atom on lattice site i respectively, $n_{i\sigma} = c^+_{i\sigma}c_{i\sigma}$ represents the density operator of fermionic atom. And $t = (4/\sqrt{\pi})E_r(V_0/E_r)^{3/4}\exp(-2(V_0/E_r)^{1/2})$ is the kinetic energy, which can be adjusted by the lattice depth V_0. $U = \sqrt{8/\pi}ka_sE_r(V_0/E_r)^{3/4}$ is the on-site interaction determined by the s-wave scattering length a_s, which can be adjusted by Feshbach resonance.

In recent experiments, the Haldane model have been realized in experiments by using laser-induce-gauge-field method in an optical lattice. This artificial gauge field proposed in Refs. [28, 29] is equinalent to a spin–orbit coupling. These systems can be described by Hamiltonian as follows:

$$H = -t\sum_{\langle ij\rangle\sigma} c^+_{i\sigma}c_{j\sigma} + \mathrm{i}\lambda\sum_{\langle ij\rangle\alpha\beta} v_{ij}c^+_i\sigma_z c_j + U\sum_i n_{i\uparrow}n_{i\downarrow} \tag{7}$$

where i, j denote the sites on lattice, $c_{i\sigma}$ is the electron annhilation operator, $n_{i\sigma} = c^+_{i\sigma}c_{i\sigma}$, t is the hopping energy, λ is spin–orbit coupling which can be adjusted by the laser-induced-gauge-field, and U is the onsite interaction.

These strongly correlated systems can be investigated by numerical methods, such as dynamical mean-field theory (DMFT) and its cluster extension, such as dynamical cluster approximation (DCA) and cellular dynamical mean-field theory (CDMFT).

3 Dynamical mean-field thory

3.1 Dynamical cluster approximation

In DCA [80, 81], the reciprocal space of the lattice containing N points is divided into finite cells [81]. The coarse-graining Green's function $\overline{G}$ is achieved by averaging Green's function G within each cell. The lattice problem is mapped into a self-consistently embedded finite-sized cluster. The coarse graining procedure of the DCA is illustrated as follows: the Brillouin zone is divided into N_c cells, and each cell is represented by a cluster momentum $\vec{\boldsymbol{K}}$. The coarse-grained Green's function is

$$\begin{aligned}\overline{G}(\vec{\boldsymbol{K}}, \mathrm{i}\omega_n) &= \frac{N_c}{N}\sum_{\tilde{\boldsymbol{k}}} G(\vec{\boldsymbol{K}} + \tilde{\boldsymbol{k}}, \mathrm{i}\omega_n) \\ &= \frac{N_c}{N}\sum_{\tilde{\boldsymbol{k}}} \frac{1}{\mathrm{i}\omega_n - \varepsilon_{\vec{\boldsymbol{K}}+\tilde{\boldsymbol{k}}} - \overline{\Sigma_\sigma}(\vec{\boldsymbol{K}}, \mathrm{i}\omega_n)}\end{aligned} \tag{8}$$

where summation over $\tilde{\boldsymbol{k}}$ is taken within the coarse-graining cell, and the ω_n is the Matsubara frequency. The self-consistent loop of DCA is shown in Fig. 5.

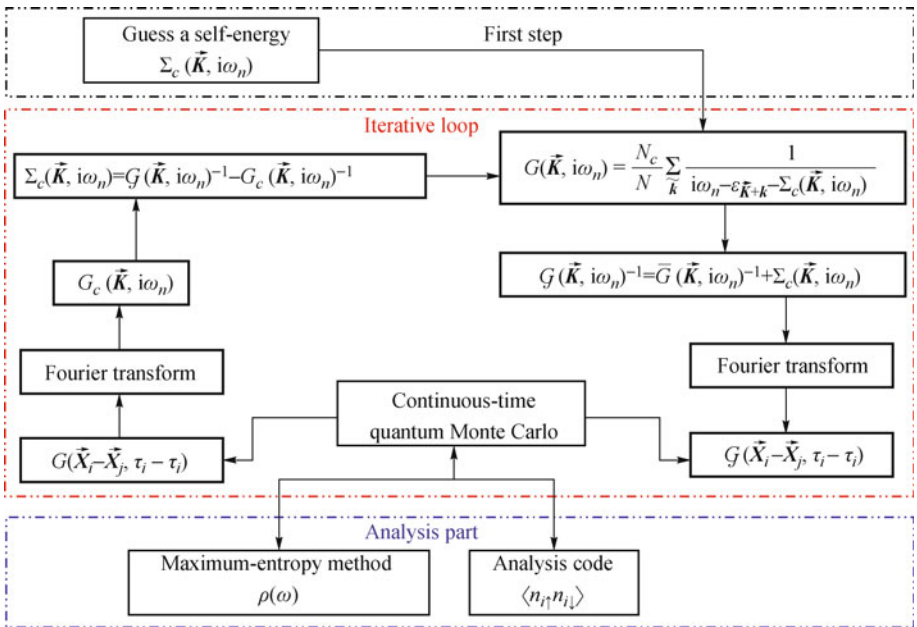

Fig. 5 Sketch of self-consistent loop of DCA. The calculation is started by guessing a self-energy, then we repeat the iterative loop part shown in the red square until reaching desired accuracy. Once the convergence is reached, by employing the analysis part shown in the blue square, we can get the lattice quantities, for example, the double occupancy and the density of states.

3.2 Cellular dynamical mean-field theory

In CDMFT [82, 83], the original lattice is mapped onto an effective cluster model via a standard DMFT procedure. The effective medium $\hat{g}$ can be got by the Dyson equation:

$$\hat{g}^{-1}(\mathrm{i}\omega_n)=\left(\sum_{\vec{K}}\frac{1}{\mathrm{i}\omega_n+\mu-\hat{t}(\vec{K})-\hat{\Sigma}(\mathrm{i}\omega_n)}\right)^{-1}+\hat{\Sigma}(\mathrm{i}\omega_n) \tag{9}$$

the $\hat{t}(\vec{K})$ is the hopping matrix in the cluster and $\vec{K}$ is taken within the reduced first Brioullion zone, $\hat{\Sigma}(\mathrm{i}\omega_n)$ is the self-energy matrix, and ω_n is the Matsubara frequency. Then, we introduce an impurity solver to solve this cluster problem, such as continuous time Monte Carlo method. The self-consistent loop of CDMFT is shown in Fig. 6.

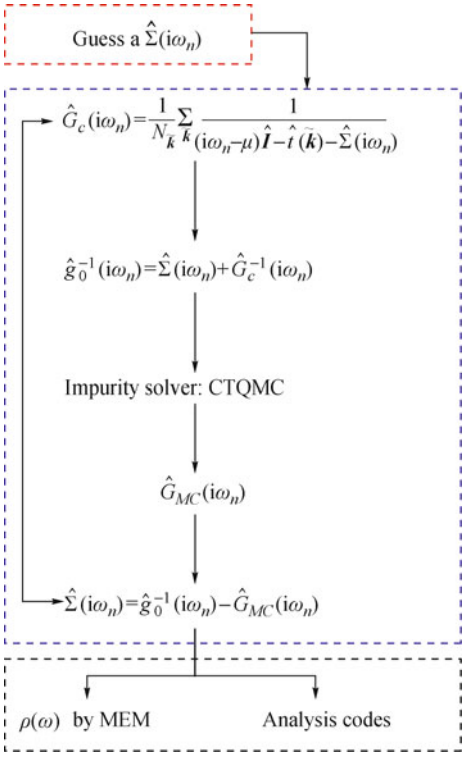

Fig. 6 Sketch of self-consistent loop of CDMFT. The calculation is started by guessing a self-energy, then the iterative loop part is repeated until desired accuracy is reached. Then, by employing the analysis part, we can get the lattice quantities, for example, the double occupancy.

4 Quantum phase transition of cold atoms

4.1 Triangular lattice

The obtained phase diagram of cold atoms trapped in triangular optical lattice is shown in Fig. 7. As the interaction increases, the system gets translated from Fermi liquid to pseudogap state. When the interaction is stronger than the critical interaction distributing on the purple line, the system gets translated from pseudogap to insulator. The phase translation line between the Fermi liquid and the pseudogap shows a reentrant behavior due to Kondo effect at low temperature. When the temperature is lower than $T/t = 2.0$, a Kondo peak emerges before the appearence of the pseudogap when the interaction increases.

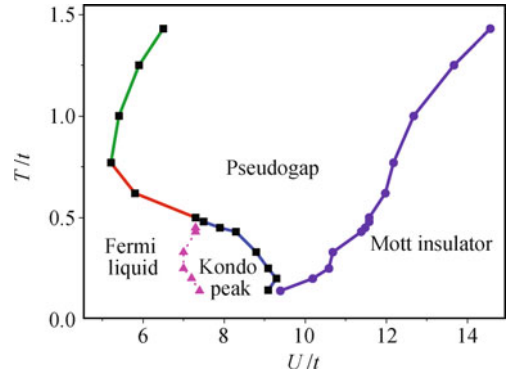

Fig. 7 The phase diagram of Fermi atoms in triangular optical lattice, where the square plots with solid line (*green*, *red*, *blue*) indicate the transition line of the Fermi liquid and the pseudogap, the circular plots with solid line (*purple*) indicate the Mott transition line, and the triangular plots with dash line (*pink*) mark the Kondo peak appearing region. Reproduced from Ref. [85], Copyright © 2010 American Physical Society.

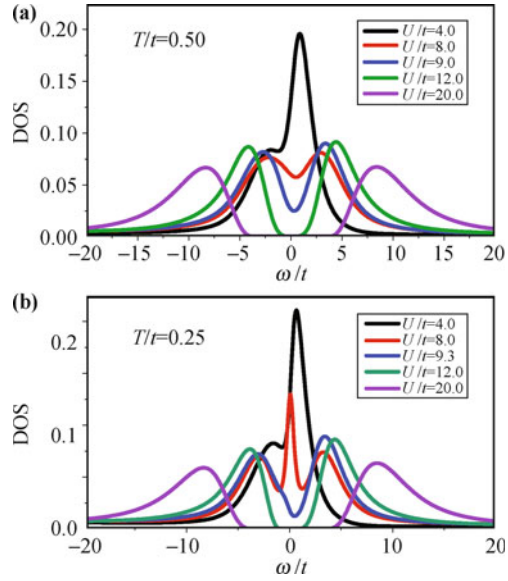

Fig. 8 The density of states (DOS) as a function of frequency ω for different interaction. **(a)** At $T/t = 0.50$, a pseudogap, formed by splitting of Fermi-liquid-like peak, appears when the interaction increases. A gap is opened when the interaction is stronger than the critical interaction $U_c/t = 11.6$. **(b)** At $T/t = 0.25$, a Kondo resonance peak is found before the pseudogap appears. Reproduced from Ref. [85], Copyright © 2010 American Physical Society.

We investigate the property of different phases mentioned above by maximum entropy method [93], which is employed to get the density of states (DOS). Fig. 8 shows the evolution of DOS with various interaction when $T/t = 0.5$ and $T/t = 0.25$. An obvious quasi-

particle peak is found when $U/t = 4.0$, which shows that the system stays at a Fermi liquid state. With the interaction, the Fermi-liquid-like peak splits into two small peaks which form a pseudogap near the Fermi energy. A gap is opened when the interaction is stronger than the critical interaction $U_c/t = 11.6$, which shows that the system becomes an insulator. When the temperature is low, as show in Fig. 8(b) when $T/t = 0.25$, a Kondo resonance peak is found before the appearence of a pseudogap near Fermi energy.

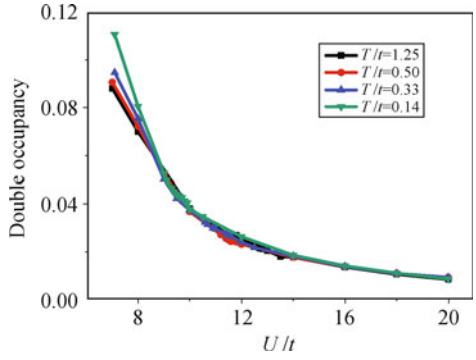

Fig. 9 The double occupancy $D_{\rm occ}$ as a function of interaction U for different temperature. Reproduced from Ref. [85], Copyright © 2010 The American Physical Society.

We also investigate the double occupancy $D_{\rm occ} = \partial F/\partial U = \frac{1}{4}\sum_i \langle n_{i\uparrow} n_{i\downarrow}\rangle$ as a function of interaction U for various temperature, where F is the free energy, as shown in Fig. 9. The $D_{\rm occ}$ decreases as the interaction increases, due to the suppressing of the itinerancy of atoms. When the interaction is stronger than the critical interaction of the Mott transition, $D_{\rm occ}$ for different temperature is almost coincident. The evolution of Fermi surface for various interaction when $T/t = 1.25$ is shown in Fig. 10. When $U/t = 5.0$, as shown in Figs. 10(a-1) and (a-2), a circular ring which implies the particles distribution on a certain energy displays a metallic behavior. When the interaction increases, the ring becomes bigger and the amplitude of the spectral weight becomes small, as shown in Figs. 10(b-1) and (b-2). Figures 10(c-1) and (c-2) show that the Fermi surface becomes a nearly flat plane, due to the localization of the particles when the interaction increases.

4.2 Honeycomb lattice

The phase diagram of interacting Dirac fermions on honeycomb lattice is showed in Fig. 11. The system undergoes a second-order Mott transition from a semi-metal state into a Mott insulator state. The critical interaction U_c decreases as the temperature T decreases, and a finite $U_c/t \sim 3.3$ for zero temperature phase transition is suggested, which agrees with the large scale quantum Monte carlo result $U_c/t \sim 3.5$ [94].

The density of states (DOS) for several interaction U at temperature $T/t = 0.05$ are presented in Fig. 12. Two quasi-particle peaks above and below Fermi level shift to the Fermi surface when the interaction increases. Spectral weight transferred to higher energy states, and eventually a gap opens at the Mott transition critical value $U_c/t \sim 3.7$. It is found that the DOS near Fermi level is independent of the interaction strength U until the Mott transition happens. We investigate the double occupancy defined by the first derivative of the free energy F, $D_{\rm occ} = \frac{\partial F}{\partial U} = \langle n_{i\uparrow} n_{i\downarrow}\rangle$ as a function of U for various temperatures. As shown in Fig. 13, when U increases, the $D_{\rm occ}$ curves decrease smoothly on the entire domain of U, which indicate second-order phase transitions. The arrows indicate the phase transition point.

Figure 14(a) shows the distribution of quasi-particles with energy $\omega/t = 0.4$ near a Dirac point $(2\sqrt{3}\pi/3,$

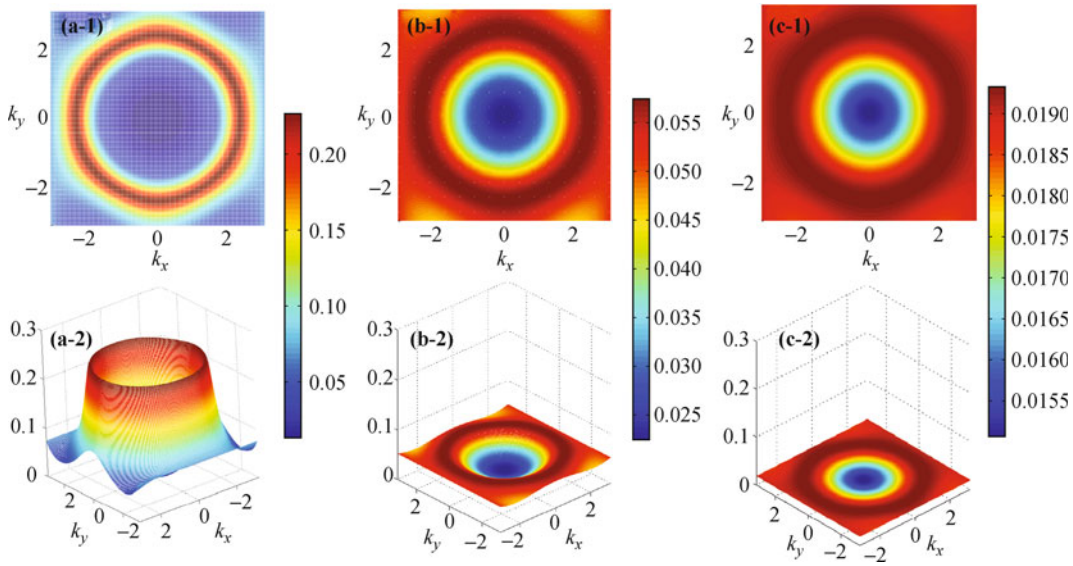

Fig. 10 The Fermi surface as a function of momentum k for different interaction at $T/t = 1.25$: **(a)** $U/t = 5.0$, **(b)** $U/t = 10.0$, **(c)** $U/t = 16.0$. Reproduced from Ref. [85], Copyright © 2010 American Physical Society.

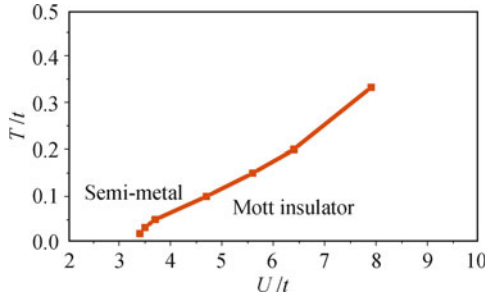

Fig. 11 Phase diagram of the interacting Dirac fermions on honeycomb lattice. The line separating the semi-metal and Mott insulator marks a second-order phase transition. Reproduced from Ref. [86], Copyright © 2010 American Physical Society.

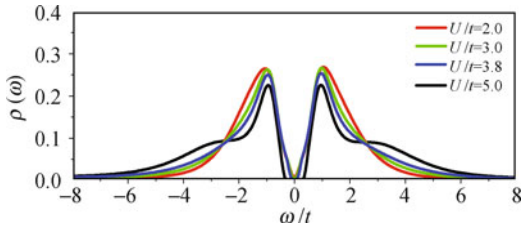

Fig. 12 The density of states for different interaction strength U at temperature $T/t = 0.05$. Within 6-site CDMFT, the DOS near Fermi level is invariable until the Mott transition happens, which denotes a constant Fermi velocity v_F in the semi-metal regime. Reproduced from Ref. [86], Copyright © 2010 American Physical Society.

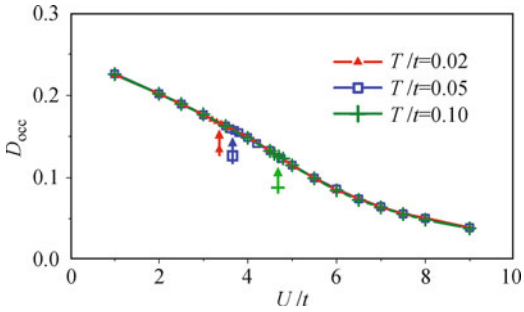

Fig. 13 Double occupancy $D_{\rm occ}$ as a function of interaction U at different temperatures. The double occupancy is insensitive to temperature for both weak- and strong-coupling regime, hence the three curves for temperature $T/t = 0.02, 0.05, 0.10$ strictly superpose each other. The double occupancies decrease smoothly as U increases, indicating second-order Mott transitions. The transition points for different temperatures are marked by the arrows. Reproduced from Ref. [86], Copyright © 2010 American Physical Society.

$2\pi/3$). When the interaction U increases, the states are being redistributed in the momentum space, although the local density of states $\rho(\omega) = \sum_k A(k,\omega)$ is independent of the interaction for small energy ω. The evolution of Fermi surface denoted by $A(k, \omega/t = 0)$ is presented in Fig. 14(b). Six Dirac points are found when $U/t = 2$. The Mott phase transition happens isochronously on six Dirac points due to the particle-hole symmetry. The locations of Dirac points are steady in momentum space when interaction U increases. When $U = 4.0$, the Fermi surface is destroyed by the interaction.

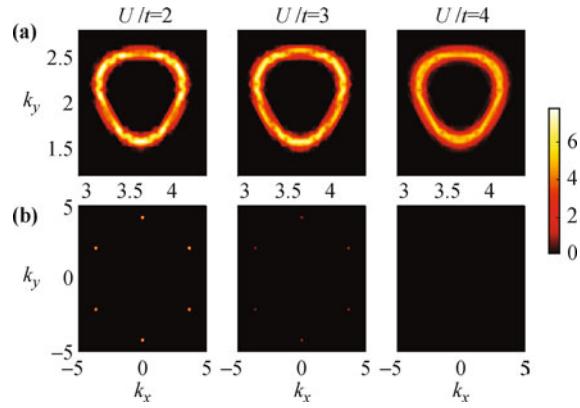

Fig. 14 The distribution of $A(k,\omega)$ in momentum space for different interactions. **(a)** The distribution of $A(k, \omega/t = 0.4)$ near a Dirac point $(2\sqrt{3}\pi/3, 2\pi/3)$ becomes isotropic in different directions when U increases. **(b)** $A(k, \omega/t = 0)$ depicts the Fermi surface of honeycomb lattice reduced to six Fermi points. Reproduced from Ref. [86], Copyright © 2010 American Physical Society.

4.3 Triangular Kagomé lattice

The triangular Kagomé lattice (TKL) can be got by inserting an extra set of triangles inside the triangles of Kagomé lattice, which has two different sublattices, shown as A-trimers and B-trimers signed by the solid circles and hollow circles respectively in Fig. 15. The phase diagram of the interacting particles on triangular Kagomé lattice is separated into metallic and insulating phases by a second-order Mott transition line, as shown in Fig. 16. The critical value U_c decreases as the

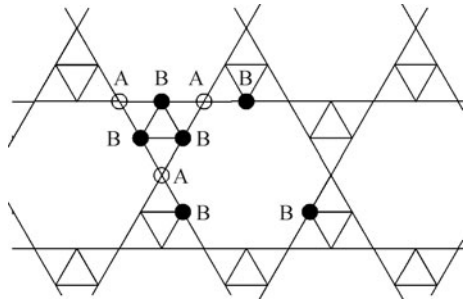

Fig. 15 The cell of triangular Kagomé lattice. The hollow circles denote the A-trimers and the black solid circles denote the B-trimers. The referenced paper is unpublished.

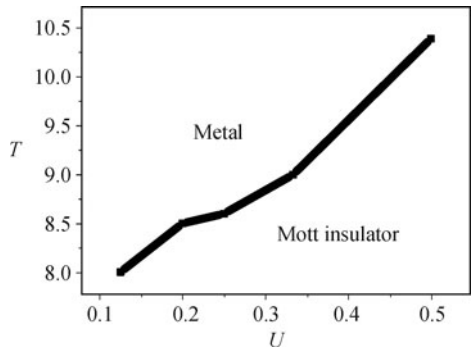

Fig. 16 The phase diagram of triangular Kagomé lattice. A second-order phase transition line separates the phase diagram into two parts signed as metal and Mott insulator. The referenced paper is unpublished.

temperature T decreases, and a finite $U_c/t \simeq 7.8$ for zero temperature phase transition is suggested.

4.4 Honeycomb lattice with spin–orbit coupling

We investigate the Kane–Mele–Hubbard model on honeycomb lattice that reads:

$$H = -t \sum_{\langle ij\rangle\sigma} c^+_{i\sigma} c_{j\sigma} + \mathrm{i}\lambda \sum_{\langle\langle ij\rangle\rangle\alpha\beta} v_{ij} c^+_{i\sigma} \sigma^z_{\alpha\beta} c_{j\sigma} + U \sum_i n_{i\uparrow} n_{i\downarrow} \quad (10)$$

where i, j label the sites on the honeycomb lattice, $c_{i\sigma}$ is the annhilation operator, $n_{i\sigma} = c^+_{i\sigma} c_{i\sigma}$, t is the hopping energy, λ is spin–orbit coupling, and U is the onsite interaction. The phase diagram of the honeycomb lattice with spin–orbit coupling is shown in Fig. 17. A semi-metal phase where the Dirac cones are preserved is found. We have observed that spin liquid phase appears at very low temperatures and the semi-metal domain prominently develops with temperature as the topological band insulator gap is also very small when $\lambda \to 0$. For $T \to 0$, the semi-metal phase reduces to a line pointing along the $\lambda = 0$ axis which survives until relatively large interactions. Both the spin liquid and topological band insulator phases at $\lambda \leqslant 0.03$ possess a small single-particle gap. In the inset of Fig. 18, we present the single particle gap and magnetization for $\lambda = 0.02$ and $T = 0.025$. The evolution of the phase diagram with temperature is shown in Fig. 18 for $\lambda = 0.02$.

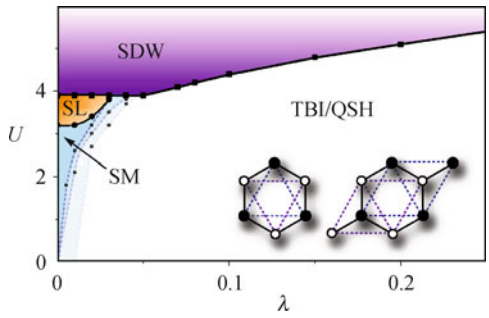

Fig. 17 Phase diagram of Kane–Mele model, including four phases: (i) topological band insulator, (ii) magnetically ordered spin density wave phase, (iii) non–magnetic insulator phase, and (iv) semi-metal region which is shown (from right to left) for temperatures $T = 0.025$, 0.0125, and 0.005. *Inset*: Typical clusters as used within cellular dynamical mean-field theory. Reproduced from Ref. [63].

We extract the edge state spectrum in the presence of interactions by computing the spectral function $A(k_y, \omega)$, as shown in Fig. 19. We have observed the following: (i) The plasmon velocity v associated with the edge modes slightly decreases for increasing U. (ii) The intensity of the spectral function decreases with increasing U. (iii) The edge modes gap out when $\langle S^x_i \rangle$ becomes finite. In Fig. 19 we show exemplarily the edge modes for fixed

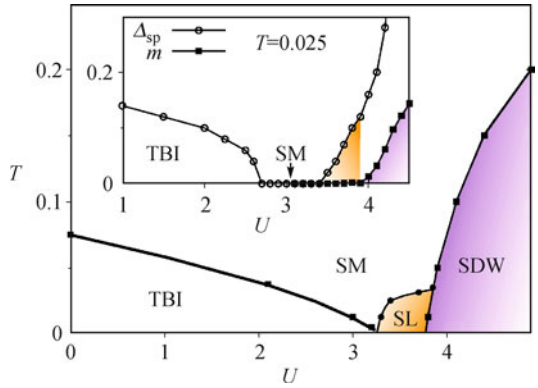

Fig. 18 Temperature dependence of the phase diagram at spin-orbital coupling $\lambda = 0.02$. *Inset*: Single-particle gap Δ_{sp} and magnetization m vs. U is shown for $\lambda = 0.02$ and $T = 0.025$. Reproduced from Ref. [63].

$\lambda = 0.2$, armchair boundary conditions, and $U = 2.0$, 3.0, and 5.2. We also compute the spectral function on a cylinder for parameters U and λ, which belongs to the spin liquid phase (see Fig. 19). While the single particle gap is very small we do not find edge states inside the gap in accordance with the spin liquid phase. We also access the double occupancy $D_{\mathrm{occ}} = \langle n_{i\uparrow} n_{i\downarrow} \rangle = \partial F/\partial U$ where F is the free energy. In Fig. 20 we show that D_{occ},

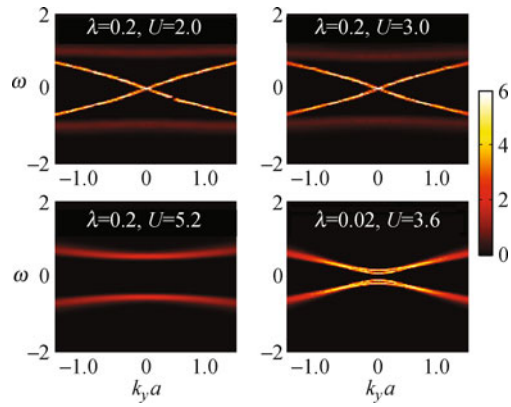

Fig. 19 Spectral function $A(k_y, \omega)$ for a cylinder geometry with armchair edges ($L = 96$). *Top*: helical edge states of the topological band insulator phase with $\lambda = 0.2$ and $U = 2.0$ or 3.0, respectively. *Bottom*, *left*: for $U = 5.2 > U_c$ (spin density wave phase) the helical edge states disappear while the single particle gap remains finite. *Bottom*, *right*: $A(k_y, \omega)$ inside the spin liquid phase: no edge states cross the gap. Reproduced from Ref. [63].

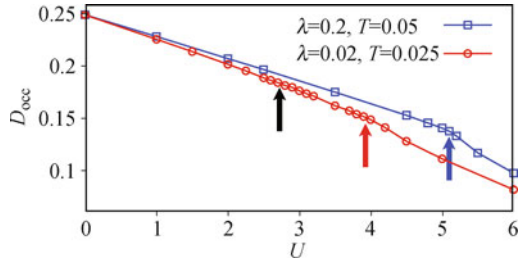

Fig. 20 Double occupancy $\langle n_{i\uparrow} n_{i\downarrow} \rangle$ as a function of U is shown for $\lambda = 0.02$ (*red circles*) and 0.2 (*blue squares*). The blue arrow (for $\lambda = 0.2$) at $U = 5.1$ and the red arrow (for $\lambda = 0.02$) at $U = 3.9$ mark the phase transition into the magnetically ordered phase. Note, the transition topological band insulator (*black arrow*) to semi-metal cannot be resolved. Reproduced from Ref. [63].

which measures the itinerant properties of electrons, is an insightful quantity to detect the magnetically ordered phase. The double occupancy is bounded as $1/4 \geqslant D_{\rm occ} \geqslant 0$. In the opposite limit, $U \to \infty$, we clearly find $D_{\rm occ} = 0$ as a fingerprint of Mott physics since we impose half filling.

4.5 Kagomé lattice with spin–orbit coupling

In comparison with the condensed matter systems, we find that detecting quantum spin Hall insulator has more advantages in optical lattice system. Due to the time-reversal symmetry, Chern number cannot be taken as a topological invariant to characterize the quantum spin Hall insulator in real electron system [95]. Chern number $C_\uparrow = +1$ ($C_\downarrow = -1$) in a quantum spin Hall phase for the up-spin (down-spin) electrons and the total Chern number $C = C_\uparrow + C_\downarrow = 0$. Since one can not distinguish the contributions of the conductance from the up or down spin electrons under current technology, it is impossible to determine whether the system is in the quantum spin Hall phase or normal phase by measuring Hall conductance. However, in cold atomic systems, it is the atom's internal states that represent the spin, not real spin, which brings certain benefits to measurement. One can directly measure the spin Chern number to determine whether the system lies in the quantum spin Hall phase or not because optically measuring the atomic internal states is very simple.

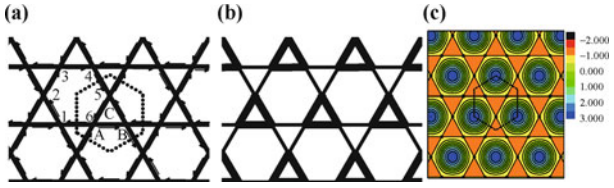

Fig. 21 **(a)** Schematic picture of the nearest neighbor intrinsic SO coupling in 2D Kagomé lattice. The up-spin atoms hop along (against) the arrowed direction with amplitude $\mathrm{i}\lambda_{\rm SO}$ ($-\mathrm{i}\lambda_{\rm SO}$). For the down-spin atoms, the arrows are reversed. The dashed line represents the Wigner–Seitz unit cell, which contains three independent sites (A, B, C). **(b)** The trimer Kagomé lattice. Hopping amplitude corresponds to $t+\kappa$ ($t-\kappa$) for the thick (thin) bonds. **(c)** Contours of the effective magnetic field for up-spin atoms defined by Eq. (11). Reproduced from Ref. [38], Copyright © 2010 American Physical Society.

The Hamiltonian is given as follows:

$$H = -t \sum_{\langle ij\rangle\sigma} c^+_{\mathrm{i}\sigma} c_{j\sigma} + \mathrm{i}\lambda \sum_{\langle ij\rangle} v_{ij} c^+_i \sigma_z c_j + \sum_{\langle ij\rangle\sigma} k_{ij} c^+_{i\sigma} c_{j\sigma} \tag{11}$$

where t is the hopping energy, λ is the spin–orbit coupling, and k_{ij} describes an alternating pattern of bond hopping integrals along the three pricipal spatial directions [see Fig. 21(b)]. For a further understanding of the topological properties of the model, we show the edge state effects in Fig. 22. From Fig. 22(a), we can see that there is a pair of chiral gapless edge states for every band gap when the SO coupling dominates. This means that the system is in topological insulator phases at 1/3- and 2/3-filling. When only the trimer term exists, it opens a band gap at Dirac point but no edge states connect the upper and lower bands [see Fig. 22(b)], therefore the system is in a normal insulator phase at 2/3-filling. On the other hand, we also see that the trimer term cannot open a gap between the bands 1 and 2 [Fig. 20(b)]. Therefore the system at 1/3-filling is still in the topological insulator phase when two perturbations are present but the trimer term dominates [see Fig. 22(c)].

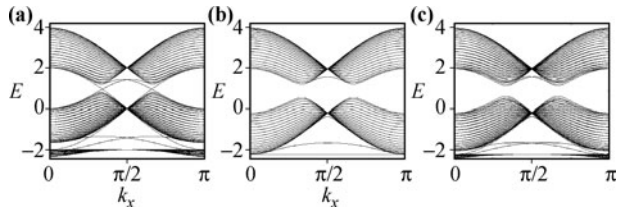

Fig. 22 The band structure of the lattice model in the stripe geometry. We take $\lambda_{\rm SO} = 0.1$, $\kappa = 0$ for **(a)**, $\lambda_{\rm SO} = 0$, $\kappa = 0.1$ for **(b)** and $\lambda_{SO} = 0.05$, $\kappa = 0.1$ for **(c)**. Reproduced from Ref. [38], Copyright 2010 American Physical Society.

Using the laser-induced-gauge-field method, one can simulate the lattice with spin–orbit coupling. It is proposed that both Abelian and non-Abelian gauge fields can be simulated in cold atomic system. In addition, the experiments to achieve such artificial gauge fields have been reported [30, 31]. Interestingly, it was proposed that a periodic magnetic field, which is not easy to be realized in a condensed-matter system, can be created by two opposite-travelling standing-wave laser beams [28, 29]. For wore information please refer to Ref. [31]. Therefore, the total effective vector potential and magnetic field can be written as

$$\begin{aligned} \boldsymbol{A}^\alpha_{\rm eff} = \alpha\hbar k_1 \{ &[\sin(2k_2 y) - \cos(k_2 y)\sin(\sqrt{k_2 x})]\mathbf{e}_x \\ &+\sqrt{3}\sin(2k_2 y)\cos(\sqrt{k_2 x})\mathbf{e}_y\} \end{aligned} \tag{12}$$

$$\boldsymbol{B}^\alpha_{\rm eff} = -\alpha\frac{2\pi\hbar k_1}{\sqrt{3}}[2\sin(k_2 y)\sin(\pi x) + \cos(2k_2 y)]\boldsymbol{e}_z \tag{13}$$

Here, $\alpha = \pm 1$ representing the up- and down-spin. The total effect field is shown in Fig. 19(c). It can be proved that this effect field equals to the SO coupling in Eq. (11).

5 Experimental protocol

We design the experimental protocol to observe the Mott transition in optical lattices. The experiment can be taken as follows: The fermionic atoms, such as ^{40}K, can be produced as a pure fermion condensate by evaporative cooling technology. Then laser beams with specific angles can be applied to set up optical lattices with different geometrical properties, such as triangular and honeycomb.

The kinetic energy t can be adjusted by the lattice depth V_0. And the Fesbbach resonance can be employed to control the on-site interaction [96–100]. In experiments, the double occupancy $D_{\rm occ}$ can be used to confirm whether the Mott transition happens. It can be carried out as follows: We rapidly increase the depth of optical lattice to prevent further tunnelling. Then the energy of atoms on doube occupied sites is shifted by Feshbach resonance. One spin component of atoms on double occupied sites is transferred to an unpopulated magnetic sublevel by a radio-frequency pulse. Then, the double occupancy can be deduced by the fraction of transformed atoms obtained by absorption imagining [20, 101]. In experiments, the Fermi surface can be detected as follows: Ramping down the optical lattice slowly enough to make the atoms stay adiabatically in the lowest band while the quasi-momentum is preserved. Then, the Fermi surface can be obtained by absorption imagining after the atoms ballistically expand for several milliseconds by completely turning off the confining potential [102, 103].

The method of detecting the quantum spin Hall phase in cold-atomic optical lattice is presented in the following. In cold atomic system, the information of quantum states is usually measured from the density profile image. So we first derive spin-atomic density from the Dirac Hamiltonian, and information of the Chern number of the system can be obtained. From the Streda formula, it has been shown that the conductivity σ_{xy} (Chern number) is related to the atomic density $\sigma_{xy}=\partial\rho/\partial\mathcal{B}|_{\mu,T}$, when a uniform magnetic field $\mathcal{B}$ is applied in the system. In optical lattice, the Chern number can be measured through the detection of the density profile [37, 62]. According to the Streda formula, one can get the relation between the spin Chern number and the spin-atomic density as

$$C_\alpha=\rho_\alpha\phi_0/\mathcal{B} \tag{14}$$

This formula provides us the approach to measure whether the system is in the quantum spin Hall phase. Firstly, we measure the spin-atomic density and denote it as $\rho^0_{\uparrow,\downarrow}$ at μ=0 in the absence of $\mathcal{B}$. Then the optical lattice is rotated to generate the effective uniform magnetic field $\mathcal{B}$, and the new density of the cold atoms $\rho^1_{\uparrow,\downarrow}$ is measured again. If $\rho^1_\uparrow > \rho^0_\uparrow$ and $\rho^1_\downarrow < \rho^0_\downarrow$, the system is in QSH insulator phase.

6 Conclusions and perspectives

In summary, we have investigated the Mott transition in several 2D optical lattices, such as triangular and honeycomb lattice which can be set up by laser beams with specific angles. As an artificial frustrated system, a reentrant behavior of the transition between Fermi liquid and pesudogap is found in triangular optical lattice due to the Kondo effect at low temperature. On honeycomb lattice, we find that low-energy density of states is independent of the interaction strength in the semimetal regime, hence the Fermi velocity always equals to the one of non-interacting Dirac sea. And the system enters Mott insulator via a second-order phase transition accompanied by a pseudogap on the Fermi surface. We also investigate the interplay between spin–orbit coupling and particle-particle interaction on honeycomb lattice. Phase diagram and temperature effects at weak spin–orbit coupling is investigated. We also propose a model including a nearest-neighbor intrinsic spin–orbit coupling and trimerized Hamiltonian in Kagomé lattice. The transition from the quantum spin Hall insulator to the normal insulator is investigated. At last, we design experimental schemes to simulate and detect the phase transition of cold atoms in optical lattices.

Acknowledgements The work was supported by the National Natural Science Foundation of China (Grant Nos. 10934010 and 60978019), the National Key Basic Research Special Foundation of China (Grant nos. 2009CB930701, 2010CB922904, 2011CB921502, and 2012CB821300), and the Research Grants Council of Hong Kong (Grant Nos. 11061160490 and 1386-N-HKU748/10).

References

1. D. Jaksch, C. Bruder, J. I. Cirac, C. W. Gardiner, and P. Zoller, Phys. Rev. Lett., 1998, 81(15): 3108
2. K. I. Petsas, A. B. Coates, and G. Grynberg, Phys. Rev. A, 1994, 50(6): 5173
3. W. Hofstetter, J. I. Cirac, P. Zoller, E. Demler, and M. D. Lukin, Phys. Rev. Lett., 2002, 89(22): 220407
4. Y. Inada, M. Horikoshi, S. Nakajima, M. Kuwata-Gonokami, M. Ueda, and T. Mukaiyama, Phys. Rev. Lett., 2008, 101(18): 180406
5. M. Kottke, T. Schulte, L. Cacciapuoti, D. Hellweg, S. Drenkelforth, W. Ertmer, and J. J. Arlt, Phys. Rev. A, 2005, 72(5): 053631
6. C. Lee, Phys. Rev. Lett., 2004, 93(12): 120406
7. X. F. Zhang, X. H. Hu, D. S. Wang, X. X. Liu, and W. M. Liu, Front. Phys., 2011, 6(1): 46
8. H. Zhai, Front. Phys. China, 2009, 4(1): 1
9. I. Bloch, J. Dalibard, and W. Zwerger, Rev. Mod. Phys., 2008, 80(3): 885
10. D. Jaksch and P. Zoller, Ann. Phys., 2005, 315(1): 52
11. L. M. Duan, E. Demler, and M. D. Lukin, Phys. Rev. Lett., 2003, 91(9): 090402
12. L. Santos, M. A. Baranov, J. I. Cirac, H. U. Everts, H. Fehrmann, and M. Lewenstein, Phys. Rev. Lett., 2004, 93(3): 030601
13. B. Damski, H. Fehrmann, H. U. Everts, M. Baranov, L. Santos, and M. Lewenstein, Phys. Rev. A, 2005, 72(5): 053612
14. B. Damski, H. U. Everts, A. Honecker, H. Fehrmann, L. Santos, and M. Lewenstein, Phys. Rev. Lett., 2005, 95(6): 060403

15. J. Ruostekoski, Phys. Rev. Lett., 2009, 103(8): 080406
16. C. Lee, T. Alexander, and Yu S. Kivshar, Phys. Rev. Lett., 2006, 97(18): 180408
17. M. Greiner, O. Mandel, T. Esslinger, T. W. Hänsch, and I. Bloch, Nature, 2002, 415(6867): 39
18. D. Hellweg, L. Cacciapuoti, M. Kottke, T. Schulte, K. Sengstock, W. Ertmer, and J. J. Arlt, Phys. Rev. Lett., 2003, 91(1): 010406
19. Y. I. Shin, C. H. Schunck, A. Schirotzek, and W. Ketterle, Nature, 2008, 451(7179): 689
20. R. Jördans, N. Strohmaier, K. Günter, H. Moritz, and T. Esslinger, Nature, 2008, 455: 204
21. N. Gemelke, X. Zhang, C. L. Hung, and C. Chin, Nature, 2009, 460(7258): 995
22. R. Jördens, L. Tarruell, D. Greif, T. Uehlinger, N. Strohmaier, H. Moritz, T. Esslinger, L. De Leo, C. Kollath, A. Georges, V. Scarola, L. Pollet, E. Burovski, E. Kozik, and M. Troyer, Phys. Rev. Lett., 2010, 104(18): 180401
23. Y. C. Zhang, G. Li, P. Zhang, J. M. Wang, and T. C. Zhang, Front. Phys. China, 2009, 4(2): 190
24. U. Schneider, L. Hackermüller, S. Will, Th. Best, I. Bloch, T. A. Costi, R. W. Helmes, D. Rasch, and A. Rosch, Science, 2009, 322(5907): 1520
25. J. Ruseckas, G. JuzeliÖas, P. Öhberg, and M. Fleischhauer, Phys. Rev. Lett., 2005, 95(1): 010404
26. K. Osterloh, M. Baig, L. Santos, P. Zoller, and M. Lewenstein, Phys. Rev. Lett., 2005, 95(1): 010403
27. G. Juzeliūnas, J. Ruseckas, P. Öhberg, and M. Fleischhauer, Phys. Rev. A, 2006, 73(2): 025602
28. S. L. Zhu, H. Fu, C. J. Wu, S. C. Zhang, and L. M. Duan, Phys. Rev. Lett., 2006, 97(24): 240401
29. S. L. Zhu, D. W. Zhang, and Z. D. Wang, Phys. Rev. Lett., 2009, 102(21): 210403
30. Y. J. Lin, R. L. Compton, A. R. Perry, W. D. Phillips, J. V. Porto, and I. B. Spielman, Phys. Rev. Lett., 2009, 102(13): 130401
31. Y. J. Lin, R. L. Compton, K. Jiménez-García, J. V. Porto, and I. B. Spielman, Nature, 2009, 462(7273): 628
32. K. v. Klitzing, G. Dorda, and M. Pepper, Phys. Rev. Lett., 1980, 45(6): 494
33. Q. Niu, D. J. Thouless, and Y. S. Wu, Phys. Rev. B, 1985, 31(6): 3372
34. T. D. Stanescu, V. Galitski, J. Y. Vaishnav, C. W. Clark, and S. D. Sarma, Phys. Rev. A, 2009, 79(5): 053639
35. A. Bermudez, N. Goldman, A. Kubasiak, M. Lewenstein, and M. A. Martin-Delgado, New J. Phys., 2010, 12(3): 033041
36. I. I. Satija, Indubala, D. C. Dakin, J. Y. Vaishnav, and C. W. Clark, Phys. Rev. A, 2008, 77(4): 043410
37. L. B. Shao, S. L. Zhu, L. Sheng, D. Y. Xing, and Z. D. Wang, Phys. Rev. Lett., 2008, 101(24): 246810
38. Guocai Liu, S. L. Zhu, Shaojian Jiang, Fadi Sun, and W. M. Liu, Phys. Rev. A, 2010, 82(5): 053605
39. X. J. Liu, X. Liu, C. Wu, and J. Sinova, Phys. Rev. A, 2010, 81(3): 033622
40. N. Goldman, I. Satija, P. Nikolic, A. Bermudez, M. A. Martin-Delgado, M. Lewenstein, and I. B. Spielman, arXiv:1002.0219v2, 2010
41. A. Bermudez, L. Mazza, M. Rizzi, N. Goldman, M. Lewenstein, and M. A. Martin-Delgado, arXiv:1004.5101v1, 2010
42. C. N. Varney, K. Sun, M. Rigol, and V. Galitski, arXiv:1007.3502v1, 2010
43. T. D. Stanescu, V. Galitski, and S. D. Sarma, arXiv:0912.3559v1, 2009
44. F. D. M. Haldane, Phys. Rev. Lett., 1988, 61(18): 2015
45. C. L. Kane and E. J. Mele, Phys. Rev. Lett., 2005, 95(14): 146802
46. C. L. Kane and E. J. Mele, Phys. Rev. Lett., 2005, 95(22): 226801
47. B. A. Bernevig, T. L. Hughes, and S. C. Zhang, Science, 2006, 314(5806): 1757
48. L. Fu, C. L. Kane, and E. J. Mele, Phys. Rev. Lett., 2007, 98(10): 106803
49. L. Fu and C. L. Kane, Phys. Rev. B, 2007, 76(4): 045302
50. J. Moore, Nat. Phys., 2009, 5(6): 378
51. J. Moore, Nature, 2009, 460(7259): 1090
52. J. E. Moore, Nature, 2010, 464(7286): 194
53. M. Büttiker, Science, 2009, 325(5938): 278
54. S. Murakami, Phys. Rev. Lett., 2006, 97(23): 236805
55. M. König, S. Wiedmann, C. Brüne, A. Roth, H. Buhmann, L. W. Molenkamp, X. L. Qi, and S. C. Zhang, Science, 2007, 318(5851): 766
56. D. Hsieh, D. Qian, L. Wray, Y. Xia, Y. S. Hor, R. J. Cava, and M. Z. Hasan, Nature, 2008, 452(7190): 970
57. P. Roushan, J. Seo, C. V. Parker, Y. S. Hor, D. Hsieh, D. Qian, A. Richardella, M. Z. Hasan, R. J. Cava, and A. Yazdani, Nature, 2009, 460(7259): 1106
58. H. Zhang, C. X. Liu, X. L. Qi, X. Dai, Z. Fang, and S. C. Zhang, Nat. Phys., 2009, 5(6): 438
59. Y. L. Chen, J. G. Analytis, J. H. Chu, Z. K. Liu, S. K. Mo, X. L. Qi, H. J. Zhang, D. H. Lu, X. Dai, Z. Fang, S. C. Zhang, I. R. Fisher, Z. Hussain, and Z. X. Shen, Science, 2009, 325(5937): 178
60. A. Sørensen, E. Demler, and M. Lukin, Phys. Rev. Lett., 2005, 94(8): 086803
61. R. N. Palmer and D. Jaksch, Phys. Rev. Lett., 2006, 96(18): 180407
62. R. O. Umucallar, H. Zhai, and M. Ö. Oktel, Phys. Rev. Lett., 2008, 100: 070402
63. W. Wu, S. Rachel, W. M. Liu, and K. Le Hur, arXiv:1106.0943, 2011
64. T. Ohashi, T. Momoi, H. Tsunetsugu, and N. Kawakami, Phys. Rev. Lett., 2008, 100(7): 076402
65. T. Yoshioka, A. Koga, and N. Kawakami, Phys. Rev. Lett., 2009, 103(3): 036401
66. D. Galanakis, T. D. Stanescu, and P. Phillips, Phys. Rev. B, 2009, 79(11): 115116
67. K. Aryanpour, W. E. Pickett, and R. T. Scalettar, Phys. Rev. B, 2006, 74(8): 085117
68. S. G. Bhongale and H. Pu, Phys. Rev. A, 2008, 78(6): 061606
69. P. B. He, Q. Sun, P. Li, S. Q. Shen, and W. M. Liu, Phys. Rev. A, 2007, 76(4): 043618
70. V. V. Konotop and M. Salerno, Phys. Rev. A, 2002, 65(2): 021602

71. Y. Kato, Q. Zhou, N. Kawashima, and N. Trivedi, Nat. Phys., 2008, 4(8): 614
72. T. Ohashi, N. Kawakami, and H. Tsunetsugu, Phys. Rev. Lett., 2006, 97(6): 066401
73. Y. Imai and N. Kawakami, Phys. Rev. B, 2002, 65(23): 233103
74. H. Lee, G. Li, and H. Monien, Phys. Rev. B, 2008, 78(20): 205117
75. X. J. Liu, X. Liu, L. C. Kwek, and C. H. Oh, Front. Phys. China, 2008, 3(2): 113
76. J. Liu and B. Liu, Front. Phys. China, 2010, 5(2): 123
77. A. Georges, G. Kotliar, W. Krauth, and M. J. Rozenberg, Rev. Mod. Phys., 1996, 68(1): 13
78. W. Metzner and D. Vollhardt, Phys. Rev. Lett., 1989, 62(3): 324
79. R. W. Helmes, T. A. Costi, and A. Rosch, Phys. Rev. Lett., 2008, 100(5): 056403
80. T. Maier, M. Jarrell, T. Pruschke, and M. H. Hettler, Rev. Mod. Phys., 2005, 77(3): 1027
81. M. Jarrell and H. R. Krishnamurthy, Phys. Rev. B, 2001, 63(12): 125102
82. G. Kotliar, S. Savrasov, G. Pálsson, and G. Biroli, Phys. Rev. Lett., 2001, 87(18): 186401
83. O. Parcollet, G. Biroli, and G. Kotliar, Phys. Rev. Lett., 2004, 92(22): 226402
84. N. H. Tong, Phys. Rev. B, 2005, 72(11): 115104
85. Y. H. Chen, W. Wu, H. S. Tao, and W. M. Liu, Phys. Rev. A, 2010, 82(4): 043625
86. W. Wu, Y. H. Chen, H. S. Tao, and W. M. Liu, Phys. Rev. B, 2010, 82(24): 245102
87. C. Chin, R. Grimm, P. Julienne, and E. Tiesinga, Rev. Mod. Phys., 2010, 82(2): 1225
88. L. M. Duan, Phys. Rev. Lett., 2005, 95(24): 243202
89. S. L. Zhu, B. G. Wang, and L. M. Duan, Phys. Rev. Lett., 2007, 98(26): 260402
90. P. Soltan-Panahi, J. Struck, P. Hauke, A. Bick, W. Plenkers, G. Meineke, C. Becker, P. Windpassinger, M. Lewenstein, and K. Sengstock, Nat. Phys., 2011, 7(5): 434
91. L. Santos, M. A. Baranov, J. I. Cirac, H. U. Everts, H. Fehrmann, and M. Lewenstein, Phys. Rev. Lett., 2004, 93(3): 030601
92. B. Damski, H. Fehrmann, H. U. Everts, M. Baranov, L. Santos, and M. Lewenstein, Phys. Rev. A, 2005, 72(5): 053612
93. M. Jarrell and J. E. Gubernatis, Phys. Rep., 1996, 269(3): 133
94. Z. Y. Meng, T. C. Lang, S. Wessel, F. F. Assaad, and A. Muramatsu, Nature, 2010, 464(7290): 847
95. D. N. Sheng, Z. Y. Weng, L. Sheng, and F. D. M. Haldane, Phys. Rev. Lett., 2006, 97(3): 036808
96. T. Loftus, C. A. Regal, C. Ticknor, J. L. Bohn, and D. S. Jin, Phys. Rev. Lett., 2002, 88(17): 173201
97. M. W. Zwierlein, A. Schirotzek, C. H. Schunck, and W. Ketterle, Science, 2006, 311(5760): 492
98. C. A. Regal, C. Ticknor, J. L. Bohn, and D. S. Jin, Nature, 2003, 424(6944): 47
99. C. Klempt, T. Henninger, O. Topic, J. Will, W. Ertmer, E. Tiemann, and J. Arlt, Phys. Rev. A, 2007, 76(2): 020701
100. T. Stöferle, H. Moritz, K. Günter, M. Köhl, and T. Esslinger, Phys. Rev. Lett., 2006, 96(3): 030401
101. N. Strohmaier, Y. Takasu, K. Günter, R. Jördens, M. Köhl, H. Moritz, and T. Esslinger, Phys. Rev. Lett., 2007, 99(22): 220601
102. M. Köhl, H. Moritz, T. Stöferle, K. Günter, and T. Esslinger, Phys. Rev. Lett., 2005, 94(8): 080403
103. J. K. Chin, D. E. Miller, Y. Liu, C. Stan, W. Setiawan, C. Sanner, K. Xu, and W. Ketterle, Nature, 2006, 443(7114): 961